

On the numerical solution to an inverse medium problem

Dinh-Liem Nguyen* Trung Truong*

Dedicated to Professor Duong Minh Duc on the occasion of his 70th birthday.

Abstract

This paper is concerned with the inverse medium problem of determining the location and shape of penetrable scattering objects from measurements of the scattered field. We study a sampling indicator function for recovering the scattering object in a fast and robust way. A flexibility of this indicator function is that it is applicable to data measured in near-field regime or far-field regime. The implementation of the function is simple and does not involve solving any ill-posed problems. The resolution analysis and stability estimate of the indicator function are investigated using the factorization analysis of the far-field operator along with the Funk-Hecke formula. The performance of the method is verified on both simulated and experimental data.

Keywords. sampling indicator function, inverse medium scattering, near-field data, Cauchy data, sampling method

AMS subject classification. 35R30, 35R09, 65R20

1 Introduction

We consider the inverse medium scattering problem for the Helmholtz equation in \mathbb{R}^n ($n = 2$ or 3). This inverse problem can be considered as a model problem for the inverse scattering of time-harmonic acoustic waves or time-harmonic TE-polarized electromagnetic waves from bounded inhomogeneous media. It has been one of the central problems in inverse scattering theory and has a wide range of applications including nondestructive testing, radar imaging, medical imaging, and geophysical exploration [8]. Needless to say, there has been a large body of literature on both theoretical and numerical studies on this inverse problem, see [6, 8] and references therein.

*Department of Mathematics, Kansas State University, Manhattan, KS 66506, USA; (dlnghuyen@ksu.edu, trungt@ksu.edu)

In the present paper, we are interested in determining the location and shape of scattering objects from (near-field or far-field) multi-static data of the scattered field. Since we study sampling methods to numerically solve this inverse problem, we will mainly discuss related results in this direction. The Linear Sampling Method (LSM) can be considered as the first sampling method developed to solve the inverse problem under consideration [7]. The LSM aims to construct an indicator function for unknown scattering objects. This indicator function is evaluated on sampling points obtained by discretizing some domain in which the unknown target is searched for. The evaluation of the indicator function is typically fast, non-iterative and its construction does not require advanced a priori information about the unknown target. These are also the main advantages of the LSM over nonlinear optimization-based methods in solving inverse scattering problems. Shortly after the finding of the LSM, other sampling type methods for inverse problems including the point source method [25], the Factorization method (FM) [18], the probe method [13] were also developed. We refer to [26] for a discussion on sampling and probe methods studied until 2006. These methods have been later extended to solve various inverse problems, see [5, 19, 26] and references therein.

Our work in this paper is inspired by a class of sampling methods that have been studied more recently. We are particularly interested in the orthogonality sampling method (OSM) proposed in [27]. While inheriting the advantages of the classical sampling methods mentioned above, the OSM is particularly attractive thanks to its simplicity and efficiency. For instance, the implementation of the OSM only involves an evaluation of an inner product or some double integral (no need to solve an ill-posed problems). The method is extremely robust with respect to noise in the data and its stability can be easily justified. However, the theoretical analysis of the OSM is far less developed compared with that of the classical sampling methods, especially the FM and LSM. We also refer to [10, 12, 14, 15, 17, 22, 24] for studies on direct sampling methods (DSM) which are closely related to the OSM.

Most of the published results on the OSM and DSM deal with the case of far-field data, see, e.g., [9, 10, 14, 22, 27] for results on the scalar Helmholtz equation and [11, 15, 20, 23] for results on the Maxwell's equations. There have been only a few results on the OSM and DSM concerning the case of near-field data. The near-field OSM studied in [1] is only applicable to the 2D case with circular measurement boundaries. The 3D case was studied in [16] under the small volume hypothesis of well-separated inhomogeneities. A flexibility of the sampling indicator function studied in this paper is that it works for near-field data (and also far-field data) and is not limited to small scatterers or 2D circular measurement boundaries. However, the method requires Cauchy data instead of only scattered field data in the near-field regime.

We analyze the sampling indicator function using the factorization analysis of the far-field operator and the Funk-Hecke formula. The idea is to relate the indicator function to $\|F\varphi_z\|^2$ where F is the far-field operator and φ_z is some special test function. Then the resolution analysis is investigated using a factorization of F , analytical properties of the operators in the factorization and the Funk-Hecke formula. To our knowledge, the idea

of combining the factorization analysis and the Funk-Hecke formula to analyze sampling indicator functions was initially introduced in [28].

The paper is organized as follows. We will formulate the inverse medium problem of interest and the factorization analysis in Section 2. The analysis and stability of the sampling indicator function is presented in Section 3. Section 4 is dedicated to a numerical study of the sampling method.

2 The inverse medium problem and the factorization analysis

In this section we formulate the inverse problem of interest and review some necessary ingredients of the factorization analysis. This factorization analysis was initially studied for the classical factorization method by Kirsch [18]. We refer to [19] for more results about the factorization method. Consider a penetrable inhomogeneous medium that occupies a bounded Lipschitz domain $D \subset \mathbb{R}^n$ ($n = 2$ or 3). Assume that this medium is characterized by the bounded function $\eta(y)$ and that $\eta = 0$ in $\mathbb{R}^n \setminus \overline{D}$. Consider the incident plane wave

$$u_{\text{in}}(x, d) = e^{ikx \cdot d}, \quad x \in \mathbb{R}^n, \quad d \in \mathbb{S}^{n-1} := \{x \in \mathbb{R}^n : |x| = 1\},$$

where $k > 0$ is the wave number and d is the direction vector of propagation. We consider the following model problem for the scattering of $u_{\text{in}}(x, d)$ by the inhomogeneous medium

$$\Delta u + k^2(1 + \eta(x))u = 0, \quad x \in \mathbb{R}^n, \quad (1)$$

$$u = u_{\text{sc}} + u_{\text{in}}, \quad (2)$$

$$\lim_{r \rightarrow \infty} r^{\frac{n-1}{2}} \left(\frac{\partial u_{\text{sc}}}{\partial r} - ik u_{\text{sc}} \right) = 0, \quad r = |x|, \quad (3)$$

where $u(x, d)$ is the total field, $u_{\text{sc}}(x, d)$ is the scattered field, and the Sommerfeld radiation condition (3) holds uniformly for all directions $x/|x| \in \mathbb{S}^{n-1}$. If $\mathbb{R}^n \setminus \overline{D}$ is connected and $\text{Im}(\eta) \geq 0$, this scattering problem is known to have a unique weak solution $u_{\text{sc}} \in H_{\text{loc}}^1(\mathbb{R}^n)$, see [8].

Inverse problem. Consider a Lipschitz domain $\Omega \subset \mathbb{R}^n$ such that $D \subset \Omega$ and denote by $\nu(x)$ the outward normal unit vector to $\partial\Omega$ at x . We aim to determine D from $u_{\text{sc}}(x, d)$ and $\partial u_{\text{sc}}(x, d)/\nu(x)$ for almost all $(x, d) \in \partial\Omega \times \mathbb{S}^{n-1}$.

We denote by $\Phi(x, y)$ the free-space Green's function of the scattering problem (1)–(3). It is well known that

$$\Phi(x, y) = \begin{cases} \frac{i}{4} H_0^{(1)}(k|x-y|), & \text{in } \mathbb{R}^2, \\ \frac{e^{ik|x-y|}}{4\pi|x-y|}, & \text{in } \mathbb{R}^3. \end{cases} \quad (4)$$

It is also well known that problem (1)–(3) is equivalent to the Lippmann-Schwinger integral equation

$$u_{\text{sc}}(x) = k^2 \int_D \Phi(x, y) \eta(y) u(y) dy, \quad (5)$$

and that the scattered field has the asymptotic behavior

$$u_{\text{sc}}(x, d) = \frac{e^{ik|x|}}{|x|^{(n-1)/2}} \left(u^\infty(\hat{x}, d) + O\left(\frac{1}{|x|}\right) \right), \quad |x| \rightarrow \infty,$$

for all $(\hat{x}, d) \in \mathbb{S}^{n-1} \times \mathbb{S}^{n-1}$. The function $u^\infty(\hat{x}, d)$ is called the scattering amplitude or the far-field pattern of the scattered field u_{sc} . Let $F : L^2(\mathbb{S}^{n-1}) \rightarrow L^2(\mathbb{S}^{n-1})$ be the far-field operator defined by

$$Fg(\hat{x}) = \int_{\mathbb{S}^{n-1}} u^\infty(\hat{x}, d) g(d) ds(d).$$

Thanks to the well-posedness of the scattering problem (1)–(3) we can define the solution operator $G : L^2(D) \rightarrow L^2(\mathbb{S}^{n-1})$ as

$$Gf = w^\infty, \quad (6)$$

where w^∞ is the scattering amplitude of the unique solution w to

$$\Delta w + k^2(1 + \eta)w = -k^2 \eta f, \quad \text{in } \mathbb{R}^n, \quad (7)$$

$$\lim_{r \rightarrow \infty} r^{\frac{n-1}{2}} \left(\frac{\partial w}{\partial r} - ikw \right) = 0, \quad r = |x|. \quad (8)$$

Note that this problem is just problem (1)–(3) rewritten for the scattered field with incident field u_{in} replaced by f . By linearity of problem (1)–(3), Fg is just the scattering amplitude of solution w to problem (7)–(8) with $f = v_g$, defined by

$$v_g(x) = \int_{\mathbb{S}^{n-1}} e^{ikx \cdot d} g(d) ds(d), \quad g \in L^2(\mathbb{S}^{n-1}), \quad x \in \mathbb{R}^n.$$

Now we define the compact operator $H : L^2(\mathbb{S}^{n-1}) \rightarrow L^2(D)$ as $Hg = v_g|_D$. Then obviously the far-field operator can be factorized as

$$F = GH.$$

Let $H^* : L^2(\mathbb{S}^{n-1}) \rightarrow L^2(\mathbb{S}^{n-1})$ be the adjoint of H given by

$$H^*g(\hat{x}) = \int_{\mathbb{S}^{n-1}} e^{-ik\hat{x} \cdot y} g(y) ds(y),$$

and we define $T : L^2(D) \rightarrow L^2(D)$ as

$$Tf = k^2 \eta(f + w), \quad (9)$$

where w solves problem (7)–(8). Since w solves the Lippmann-Schwinger equation $w(x) = k^2 \int_D \Phi(x, y) \eta(y) (w(y) + f(y)) dy$, we can deduce from scattering amplitude of w that (see [4])

$$G = H^*T, \quad F = H^*TH.$$

To proceed further with the analysis of the Factorization method we need to briefly discuss the interior transmission eigenvalues. We call $k > 0$ an interior transmission eigenvalue if the problem

$$\begin{aligned} \Delta u + k^2(1 + \eta)u &= 0, & \text{in } D \\ \Delta v + k^2v &= 0, & \text{in } D \\ u = v, \quad \frac{\partial u}{\partial \nu} &= \frac{\partial v}{\partial \nu}, & \text{on } \partial D \end{aligned}$$

has a nontrivial solution $(u, v) \in L^2(D) \times L^2(D)$ such that $u - v \in H^2(D)$.

We refer to [4] and the references therein for more details about transmission eigenvalues. For the next results, we assume that k is not an interior transmission eigenvalue. The following assumption is also important for the factorization analysis.

Assumption 1. *We assume that $\eta \in L^\infty(\mathbb{R}^n)$, $\text{Im}(\eta) \geq 0$ and that there exists a constant $c > 0$ such that $\text{Re}(\eta(x)) + \text{Im}(\eta(x)) \geq c$ for almost all $x \in D$.*

The following theorem of the factorization analysis is important to the sampling method studied in the next section, see [2] for a proof of the theorem.

Theorem 2. *If Assumption 1 holds true, then operator T defined in (9) satisfies the coercivity property. That means there exists a constant $\gamma > 0$ such that*

$$|\langle Tf, f \rangle| \geq \gamma \|f\|^2, \quad \text{for all } f \in \text{Range}(H).$$

3 A sampling indicator function

In this section we introduce the sampling indicator function and analyze its properties. We define the indicator function $I(z)$ as

$$I(z) := \int_{\mathbb{S}^{n-1}} \left| \int_{\mathbb{S}^{n-1}} \int_{\partial\Omega} u_{\text{sc}}(y, d) \frac{\partial \Phi^\infty(\hat{x}, y)}{\partial \nu(y)} - \frac{\partial u_{\text{sc}}(y, d)}{\partial \nu(y)} \Phi^\infty(\hat{x}, y) ds(y) \varphi_z(d) ds(d) \right|^2 ds(\hat{x}) \quad (10)$$

where φ_z is given by

$$\varphi_z(d) = e^{-ikd \cdot z}, \quad d \in \mathbb{S}^{n-1}, \quad z \in \mathbb{R}^n, \quad (11)$$

and $\Phi^\infty(\hat{x}, y)$ is the scattering amplitude of the Green's function $\Phi(x, y)$, given by

$$\Phi^\infty(\hat{x}, y) = \begin{cases} \frac{e^{i\pi/4}}{\sqrt{8\pi k}} e^{-ik\hat{x} \cdot y}, & \text{in } \mathbb{R}^2, \\ \frac{1}{4\pi} e^{-ik\hat{x} \cdot y}, & \text{in } \mathbb{R}^3. \end{cases}$$

Recall that J_0 and j_0 are respectively a Bessel function and a spherical Bessel function of the first kind. The behavior of $I(z)$ is analyzed in the following theorem.

Theorem 3. *Assume that k is not an interior transmission eigenvalue and that Assumption 1 holds true. Then the indicator function $I(z)$ satisfies*

$$0 < \frac{\gamma^2}{|\mathbb{S}^{n-1}|} \left(\int_D |\alpha_z(x)|^2 dx \right)^2 \leq I(z) \leq \|G\|^2 \int_D |\alpha_z(x)|^2 dx, \quad z \in \mathbb{R}^n, \quad (12)$$

where γ is the positive constant in the coercivity of operator T in Theorem 2, G is the solution operator defined in (6), and

$$\alpha_z(x) = \begin{cases} 2\pi J_0(k|z-x|), & \text{in } \mathbb{R}^2, \\ 4\pi j_0(k|z-x|), & \text{in } \mathbb{R}^3. \end{cases}$$

Furthermore

$$I(z) = O\left(\frac{1}{\text{dist}(z, D)^{n-1}}\right) \quad \text{as } \text{dist}(z, D) \rightarrow \infty, \quad (13)$$

where $\text{dist}(z, D)$ is the distance from z to D .

Remark 4. *From the behavior of the Bessel functions J_0 and j_0 we know that $|\alpha_z(x)|^2$ peaks as sampling point z approaches point x in the scatterer D and that $|\alpha_z(x)|^2$ decays as z is away from x with the decay rate (13). We thus expect from the upper bound in (12) that $I(z)$ takes small values as z is outside D . From the lower bound in (12), $I(z)$ is bounded by a positive constant as z is inside D . This is not a rigorous justification for the behavior of $I(z)$. Such a justification is still an open problem.*

Proof. From the Helmholtz integral representation for u_{sc} (see [8]) we have

$$u_{\text{sc}}(x, d) = \int_{\partial\Omega} u_{\text{sc}}(y, d) \frac{\partial\Phi(x, y)}{\partial\nu(y)} - \frac{\partial u_{\text{sc}}(y, d)}{\partial\nu(y)} \Phi(x, y) ds(y).$$

This deduces that

$$u^\infty(\hat{x}, d) = \int_{\partial\Omega} u_{\text{sc}}(y, d) \frac{\partial\Phi^\infty(\hat{x}, y)}{\partial\nu(y)} - \frac{\partial u_{\text{sc}}(y, d)}{\partial\nu(y)} \Phi^\infty(\hat{x}, y) ds(y).$$

Then substituting this formula of u^∞ in the far-field operator F implies that

$$F\varphi_z(\hat{x}) = \int_{\mathbb{S}^{n-1}} \int_{\partial\Omega} u_{\text{sc}}(y, d) \frac{\partial\Phi^\infty(\hat{x}, y)}{\partial\nu(y)} - \frac{\partial u_{\text{sc}}(y, d)}{\partial\nu(y)} \Phi^\infty(\hat{x}, y) ds(y) \varphi_z(d) ds(d).$$

Therefore we derive from the definition of $I(z)$ that

$$I(z) = \int_{\mathbb{S}^{n-1}} |F\varphi_z(\hat{x})|^2 ds(\hat{x}) = \|F\varphi_z\|^2.$$

Since $\|\varphi_z\|^2 = \int_{\mathbb{S}^{n-1}} |e^{-ikz \cdot d}|^2 ds(d) = |\mathbb{S}^{n-1}|$ (the surface area of \mathbb{S}^{n-1}), using the Cauchy-Schwarz inequality and the factorization of the far-field operator F we obtain

$$\sqrt{|\mathbb{S}^{n-1}|} \|F\varphi_z\| \geq \langle F\varphi_z, \varphi_z \rangle = \langle H^*TH\varphi_z, \varphi_z \rangle = \langle TH\varphi_z, H\varphi_z \rangle.$$

Using the coercivity of T in Theorem 2 and $\|F\varphi_z\| \leq \|G\| \|H\varphi_z\|$ implies that

$$\frac{\gamma^2}{|\mathbb{S}^{n-1}|} \|H\varphi_z\|^4 \leq I(z) \leq \|G\|^2 \|H\varphi_z\|^2,$$

where γ is the constant from the coercivity of T in Theorem 2.

Now using the Funk-Hecke formula (see [8]) we obtain

$$H\varphi_z(x) = \int_{\mathbb{S}^{n-1}} e^{-ik(z-x) \cdot d} ds(d) = \begin{cases} 2\pi J_0(k|z-x|), & \text{in } \mathbb{R}^2, \\ 4\pi j_0(k|z-x|), & \text{in } \mathbb{R}^3, \end{cases} \quad (14)$$

which allows us to establish the estimate in (12). The strict positivity of the lower bound in the estimate can be deduced from the fact that the operator H is an injective operator, see [2]. Finally, using the asymptotic behavior of $J_0(r) = O(1/\sqrt{r})$ and $j_0(r) = O(1/r)$ as $r \rightarrow \infty$ we obtain that

$$\|H\varphi_z\|^2 = O\left(\frac{1}{\text{dist}(z, D)^{n-1}}\right), \quad \text{as } \text{dist}(z, D) \rightarrow \infty.$$

This completes the proof. \square

In practice the data are always perturbed with some noise. We assume the noisy data u_{sc}^δ and $\partial u_{\text{sc}}^\delta / \partial \nu$ satisfy

$$\|u_{\text{sc}} - u_{\text{sc}}^\delta\|_{L^2(\partial\Omega \times \mathbb{S}^{n-1})} \leq \delta_1 \|u_{\text{sc}}\|_{L^2(\partial\Omega \times \mathbb{S}^{n-1})}, \quad (15)$$

$$\left\| \frac{\partial u_{\text{sc}}}{\partial \nu} - \frac{\partial u_{\text{sc}}^\delta}{\partial \nu} \right\|_{L^2(\partial\Omega \times \mathbb{S}^{n-1})} \leq \delta_2 \left\| \frac{\partial u_{\text{sc}}}{\partial \nu} \right\|_{L^2(\partial\Omega \times \mathbb{S}^{n-1})}, \quad (16)$$

for some positive constants δ_1, δ_2 . We now prove a stability estimate for the indicator function $I(z)$.

Theorem 5. *Denote by $I^\delta(z)$ the indicator function corresponding to noisy data u_{sc}^δ and $\partial u_{\text{sc}}^\delta / \partial \nu$. Then*

$$|I(z) - I^\delta(z)| \leq \mathcal{C} (2 \max(\delta_1, \delta_2) + \max(\delta_1^2, \delta_2^2)), \quad \text{for all } z \in \mathbb{R}^3,$$

where

$$\mathcal{C} = |\mathbb{S}^{n-1}|^2 \left(\|\Phi^\infty\|_{L^2(\mathbb{S}^{n-1} \times \partial\Omega)}^2 + \left\| \frac{\partial \Phi^\infty}{\partial \nu} \right\|_{L^2(\mathbb{S}^{n-1} \times \partial\Omega)}^2 \right) \left(\|u_{\text{sc}}\|_{L^2(\partial\Omega \times \mathbb{S}^{n-1})}^2 + \left\| \frac{\partial u_{\text{sc}}}{\partial \nu} \right\|_{L^2(\partial\Omega \times \mathbb{S}^{n-1})}^2 \right).$$

Proof. Let $u^{\infty,\delta}(\hat{x}, d)$ and F^δ be the scattering amplitude and the far-field operator for noisy Cauchy data. That means

$$u^{\infty,\delta}(\hat{x}, d) = \int_{\partial\Omega} u_{\text{sc}}^\delta(y, d) \frac{\partial\Phi^\infty(\hat{x}, y)}{\partial\nu(y)} - \frac{\partial u_{\text{sc}}^\delta(y, d)}{\partial\nu(y)} \Phi^\infty(\hat{x}, y) ds(y) \quad (17)$$

$$F^\delta \varphi_z(\hat{x}) = \int_{\mathbb{S}^{n-1}} u^{\infty,\delta}(\hat{x}, d) \varphi_z(d) ds(d). \quad (18)$$

Using the Cauchy-Schwarz inequality we have

$$|u^\infty(\hat{x}, d) - u^{\infty,\delta}(\hat{x}, d)| \leq \|(u_{\text{sc}} - u_{\text{sc}}^\delta)(\cdot, d)\| \left\| \frac{\partial\Phi^\infty(\hat{x}, \cdot)}{\partial\nu(\cdot)} \right\| + \left\| \frac{\partial(u_{\text{sc}} - u_{\text{sc}}^\delta)(\cdot, d)}{\partial\nu(\cdot)} \right\| \|\Phi^\infty(\hat{x}, \cdot)\|,$$

and hence

$$\begin{aligned} & |u^\infty(\hat{x}, d) - u^{\infty,\delta}(\hat{x}, d)|^2 \\ & \leq \left(\|(u_{\text{sc}} - u_{\text{sc}}^\delta)(\cdot, d)\|^2 + \left\| \frac{\partial(u_{\text{sc}} - u_{\text{sc}}^\delta)(\cdot, d)}{\partial\nu(\cdot)} \right\|^2 \right) \left(\|\Phi^\infty(\hat{x}, \cdot)\|^2 + \left\| \frac{\partial\Phi^\infty(\hat{x}, \cdot)}{\partial\nu(\cdot)} \right\|^2 \right). \end{aligned}$$

Let $C = \|\Phi^\infty\|_{L^2(\mathbb{S}^{n-1} \times \partial\Omega)}^2 + \|\partial\Phi^\infty/\partial\nu\|_{L^2(\mathbb{S}^{n-1} \times \partial\Omega)}^2$. This leads to

$$\begin{aligned} \|u^\infty - u^{\infty,\delta}\|_{L^2(\mathbb{S}^{n-1} \times \mathbb{S}^{n-1})}^2 & \leq C \left(\|(u_{\text{sc}} - u_{\text{sc}}^\delta)\|_{L^2(\partial\Omega \times \mathbb{S}^{n-1})}^2 + \left\| \frac{\partial(u_{\text{sc}} - u_{\text{sc}}^\delta)}{\partial\nu} \right\|_{L^2(\partial\Omega \times \mathbb{S}^{n-1})}^2 \right) \\ & \leq C \left(\delta_1^2 \|u_{\text{sc}}\|_{L^2(\partial\Omega \times \mathbb{S}^{n-1})}^2 + \delta_2^2 \left\| \frac{\partial u_{\text{sc}}}{\partial\nu} \right\|_{L^2(\partial\Omega \times \mathbb{S}^{n-1})}^2 \right), \end{aligned}$$

which implies that

$$\|F\varphi_z - F^\delta\varphi_z\|^2 \leq C|\mathbb{S}^{n-1}|^2 \max(\delta_1^2, \delta_2^2) \left(\|u_{\text{sc}}\|_{L^2(\partial\Omega \times \mathbb{S}^{n-1})}^2 + \left\| \frac{\partial u_{\text{sc}}}{\partial\nu} \right\|_{L^2(\partial\Omega \times \mathbb{S}^{n-1})}^2 \right).$$

Similarly we also have

$$\|F\varphi_z\|^2 \leq C|\mathbb{S}^{n-1}|^2 \left(\|u_{\text{sc}}\|_{L^2(\partial\Omega \times \mathbb{S}^{n-1})}^2 + \left\| \frac{\partial u_{\text{sc}}}{\partial\nu} \right\|_{L^2(\partial\Omega \times \mathbb{S}^{n-1})}^2 \right).$$

Using $I(z) = \|F\varphi_z\|^2$ and the triangle inequality we have

$$\begin{aligned} |I(z) - I^\delta(z)| & = \left| \|F\varphi_z\|^2 - \|F^\delta\varphi_z\|^2 \right| \leq \|F\varphi_z - F^\delta\varphi_z\| (\|F\varphi_z\| + \|F^\delta\varphi_z\|) \\ & \leq 2\|F\varphi_z\| \|F\varphi_z - F^\delta\varphi_z\| + \|F\varphi_z - F^\delta\varphi_z\|^2 \\ & \leq C|\mathbb{S}^{n-1}|^2 \left(\|u_{\text{sc}}\|_{L^2(\partial\Omega \times \mathbb{S}^{n-1})}^2 + \left\| \frac{\partial u_{\text{sc}}}{\partial\nu} \right\|_{L^2(\partial\Omega \times \mathbb{S}^{n-1})}^2 \right) \left(2\sqrt{\max(\delta_1^2, \delta_2^2)} + \max(\delta_1^2, \delta_2^2) \right). \end{aligned}$$

proving the theorem. \square

Remark 6. We note that if the far-field measurements are taken on the boundary of the ball of large radius R , by the radiation condition we can approximate $\partial u_{\text{sc}}/\partial \nu$ by iku_{sc} in $I(z)$. Then the modified indicator function

$$I_{\text{far}}(z) := \int_{\mathbb{S}^{n-1}} \left| \int_{\mathbb{S}^{n-1}} \int_{\partial\Omega} u_{\text{sc}}(y, d) \frac{\partial \Phi^\infty(\hat{x}, y)}{\partial \nu(y)} - iku_{\text{sc}}(y, d) \Phi^\infty(\hat{x}, y) ds(y) \varphi_z(d) ds(d) \right|^2 ds(\hat{x}) \quad (19)$$

only needs the scattered field data $u_{\text{sc}}(x, d)$ and approximates the indicator function $I(z)$.

4 Numerical study

In this section we study the numerical performance of the sampling method for both simulated and experimental data in two dimensions. More precisely, for simulated data, we will examine the performance of the method for data with different wave numbers (Figure 1), highly noisy data (Figure 2), far-field data (Figure 3), and limited aperture data (Figure 4). Reconstruction results using the indicator function $I_{\text{far}}(z)$ are also presented in the case of far-field data. For experimental data, we apply the indicator function $I_{\text{far}}(z)$ to three data sets of dielectric and metallic objects from the Fresnel Institute (Figure 5). For the pictures in this section, the indicator functions are scaled by dividing by their maximal values.

The following common parameters and notations are used in the numerical examples of simulated data

$$\begin{aligned} \text{Sampling domain} &= (-2, 2) \times (-2, 2), \\ \text{Number of sampling points} &= 96^2, \\ \partial\Omega &= \{(x_1, x_2)^\top \in \mathbb{R}^2 : x_1^2 + x_2^2 = R^2\}, \\ \text{Near-field data: } R &= 3, \\ \text{Far-field data: } R &= 100, \\ \text{Number of data points on } \partial\Omega &: N_x, \\ \text{Number of incident plane waves: } &N_d. \end{aligned}$$

The following scattering objects are considered in the numerical examples.

a) Kite-shaped object

$$\begin{aligned} \partial D &= \{x \in \mathbb{R}^2 : x = ((\cos(t) + 0.65 \cos(2t) - 0.65)/2, 1.5 \sin(t)/2.5)^\top, 0 \leq t \leq 2\pi\}, \\ \eta(x) &= 0.5 + 0.1i \quad \text{in } D. \end{aligned}$$

b) Disk-and-rectangle object

$$\begin{aligned} \text{disk} &= \{(x_1, x_2)^\top \in \mathbb{R}^2 : (x_1 + 0.6)^2 + (x_2 - 0.6)^2 < 0.4^2\}, \\ \text{rectangle} &= \{(x_1, x_2)^\top \in \mathbb{R}^2 : |x_1 - 0.6| < 0.45, |x_2 + 0.6| < 0.25\}, \\ D &= \text{disk} \cup \text{rectangle}, \\ \eta(x) &= 0.5 \quad \text{in } D. \end{aligned}$$

c) Square-shaped object with cavity

$$\begin{aligned} \text{cavity} &= \{(x_1, x_2)^\top \in \mathbb{R}^2 : x_1^2 + x_2^2 < 0.3^2\}, \\ \text{square} &= \{(x_1, x_2)^\top \in \mathbb{R}^2 : |x_1| < 0.5, |x_2| < 0.5\}, \\ D &= \text{square} \setminus \overline{\text{cavity}}, \\ \eta(x) &= 1 \quad \text{in } D. \end{aligned}$$

To generate the scattering data for the numerical examples, we solve the Lippmann-Schwinger equation (5) using a spectral Galerkin method developed in [21]. Using N_d incident plane waves and measuring the data at N_x points on $\partial\Omega$, the Cauchy data $u_{\text{sc}}(x, d), \partial u_{\text{sc}}/\partial\nu(x, d)$, where $(x, d) \in \partial\Omega \times \mathbb{S}$, are then $N_d \times N_x$ matrices. The artificial noise is added to the data as follows. Two complex-valued noise matrices $\mathcal{N}_{1,2}$ containing random numbers that are uniformly distributed in the complex square

$$\{a + ib : |a| \leq 1, |b| \leq 1\} \subset \mathbb{C}$$

are added to the data matrices. For simplicity we consider the same noise level δ for both u_{sc} and $\partial u_{\text{sc}}/\partial\nu$. The noisy data u_{sc}^δ and $\partial u_{\text{sc}}^\delta/\partial\nu$ are given by

$$u_{\text{sc}}^\delta := u_{\text{sc}} + \delta \frac{\mathcal{N}_1}{\|\mathcal{N}_1\|_F} \|u_{\text{sc}}\|_F, \quad \frac{\partial u_{\text{sc}}^\delta}{\partial\nu} := \frac{\partial u_{\text{sc}}}{\partial\nu} + \delta \frac{\mathcal{N}_2}{\|\mathcal{N}_2\|_F} \left\| \frac{\partial u_{\text{sc}}}{\partial\nu} \right\|_F,$$

where $\|\cdot\|_F$ is the Frobenius matrix norm.

4.1 Reconstruction with different wave numbers (Figure 1)

We present in Figure 2 reconstruction results for the wave numbers $k = 4$ (wavelength ≈ 1.57) and $k = 8$ (wavelength ≈ 0.78). The data are near-field Cauchy data with 30% noise. We use $N_x \times N_d = 64 \times 64$ for the kite-shaped object and disk-and-rectangle object, while the square-shaped object with cavity is examined with $N_x \times N_d = 96 \times 96$. It can be seen from the Figure 1 that the reconstruction results are improved with a larger value of k . We also see that the two imaging functionals can image very well the square-shaped object with cavity. It is interesting that this object violates the assumption that $\mathbb{R}^n \setminus \overline{D}$ must be connected when studying the well-posedness of the direct scattering problem (1)–(3).

4.2 Reconstruction with highly noisy data (Figure 2)

We present in Figure 2 reconstruction results for near-field Cauchy data perturbed by 60% and 90% noise. The wave number $k = 8$ and again we use $N_x \times N_d = 64 \times 64$ for the kite-shaped object and disk-and-rectangle object, and $N_x \times N_d = 96 \times 96$ for the square-shaped object with cavity. Although we can notice some deterioration in the case of 90% noise, the reconstructions are still pretty reasonable. These results show that the sampling method is extremely robust with respect to noise in the data. We have also observed this robustness in the orthogonality sampling method for Maxwell's equations, see [11].

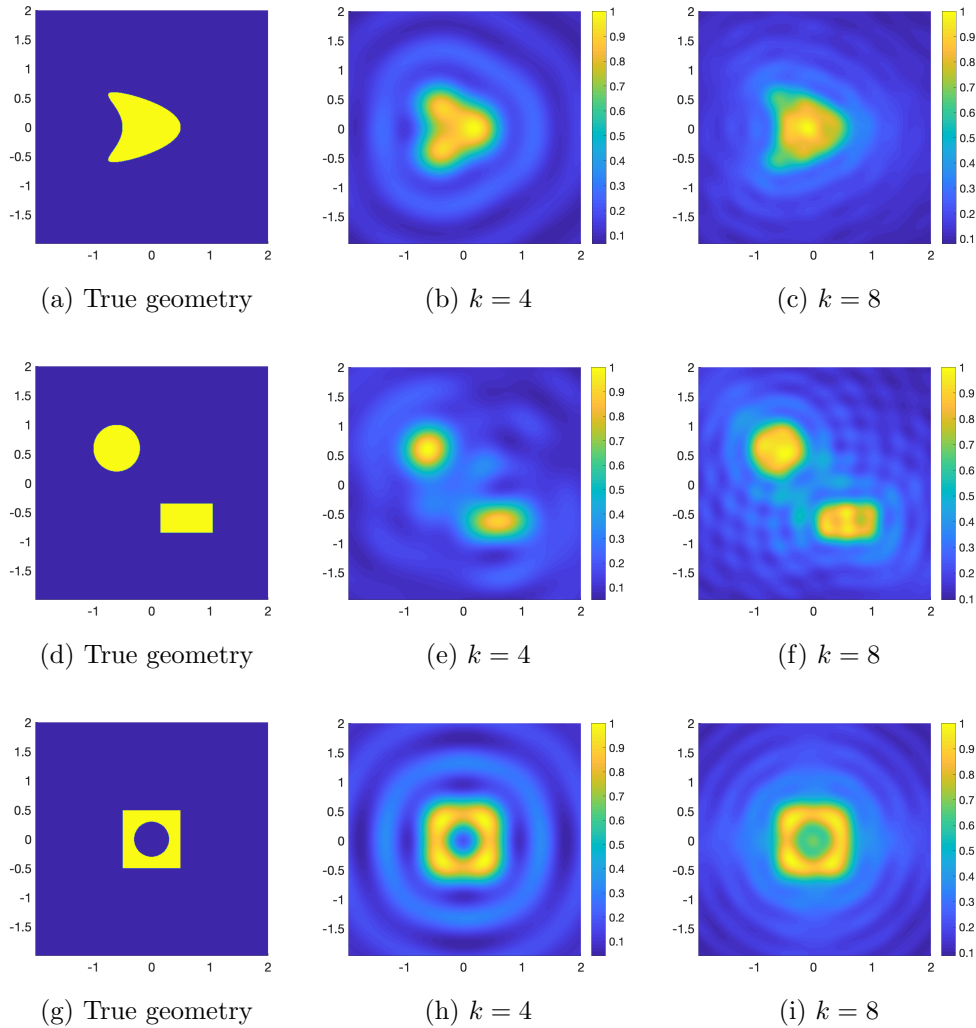


Figure 1: Reconstruction with near-field Cauchy data for different wave numbers. There is 30% noise added to the data ($\delta = 0.3$). First column (a, d, g): true geometry. Second column (b, e, h): reconstruction with $k = 4$. Third column (c, f, i): reconstruction with $k = 8$.

4.3 Reconstruction with far-field data (Figure 3)

The focus of this example is to examine the performance of the sampling methods associated with $I(z)$ and $I_{\text{far}}(z)$, defined by (19), in the case of far-field data with 30% noise. We recall that $I_{\text{far}}(z)$ uses only u_{sc} instead of the Cauchy data. Again we consider $k = 8$ and the size $N_x \times N_d$ of the data matrices are the same as in the previous examples. As mentioned at the beginning of this section the far-field data are measured on $\partial\Omega$ that is the circle of radius $R = 100$ (about 125 wavelengths away from the scattering objects). We can see in Figure 3 that the reconstruction results with far-field data are as good

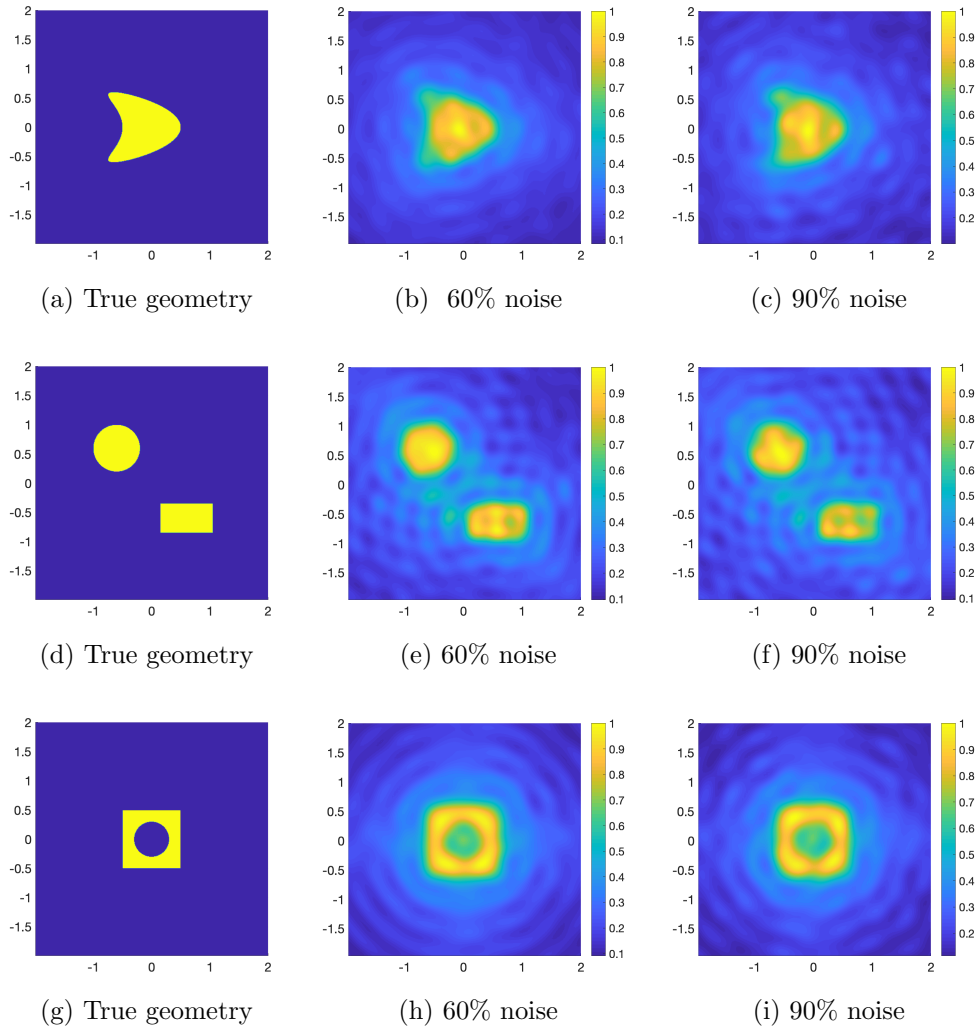


Figure 2: Reconstruction with highly noisy near-field data. Wave number $k = 8$. First column (a, d, g): true geometry. Second column (b, e, h): reconstruction with 60% noise. Third column (c, f, i): reconstruction with 90% noise.

as those with the near-field data. The two imaging functionals $I(z)$ and $I_{\text{far}}(z)$ provide similar results as expected.

4.4 Reconstruction with limited aperture data (Figure 4)

In this last example we consider near-field data for a half-circle aperture (30% noise). More precisely, the incident point sources are located on the upper half the measurement circle $\partial\Omega$, and the Cauchy data are given on the bottom half of $\partial\Omega$. Moreover, the number of data points N_x and incident plane waves N_d are also half of those of the full data case, that means $N_x \times N_d = 32 \times 32$ for the kite-shaped object and disk-and-rectangle object,

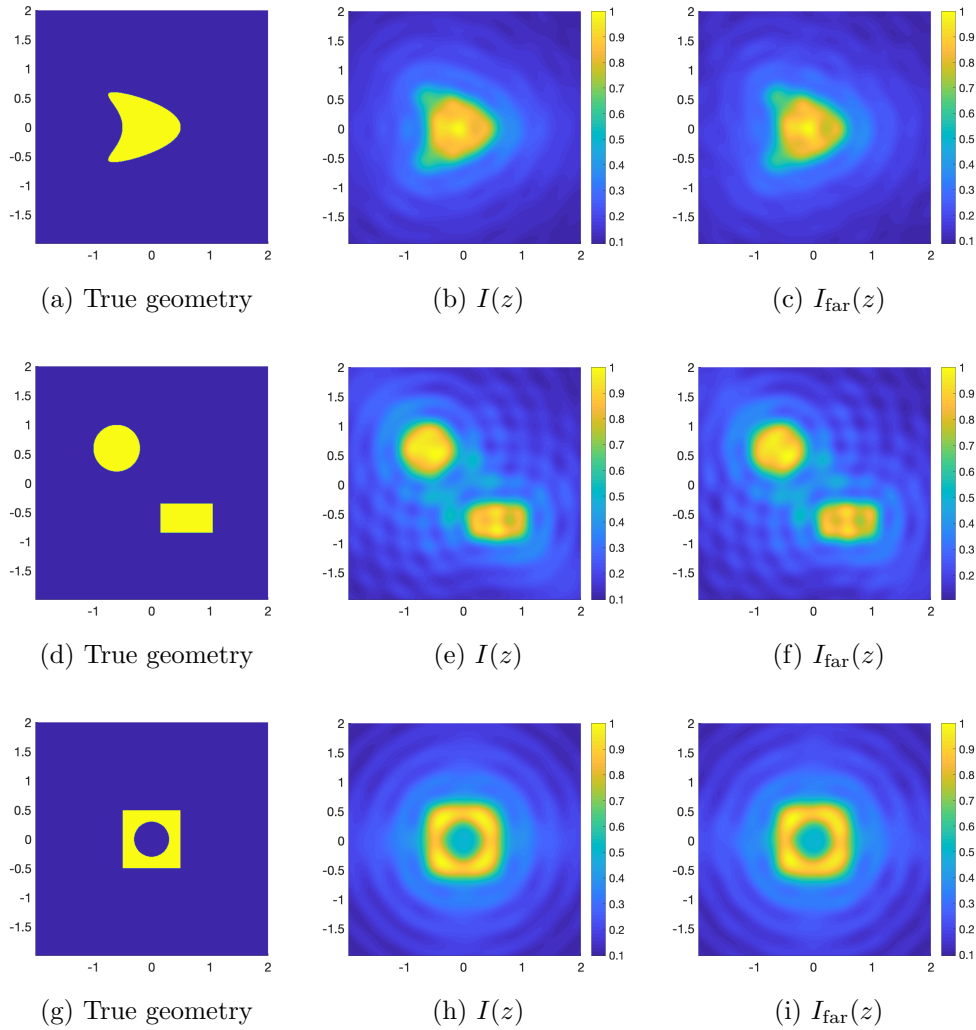


Figure 3: Reconstruction with far-field data. There is 30% noise added to the data, $k = 8$. First column (a, d, g): true geometry. Second column (b, e, h): reconstruction using $I(z)$. Third column (c, f, i): reconstruction using $I_{\text{far}}(z)$.

and $N_x \times N_d = 48 \times 48$ for the square-shaped object with cavity. As it can be seen from Figure 4, the reconstruction results for the the first two objects are still pretty reasonable. However, the shape of the reconstructed square-shaped object with cavity is no longer accurate. This object is certainly more difficult to image compared with the first two objects.

4.5 Reconstruction with experimental data (Figure 5)

In this section we verify the performance of the indicator function with experimental data provided by Institut Fresnel (France). We used the data sets of homogeneous objects.

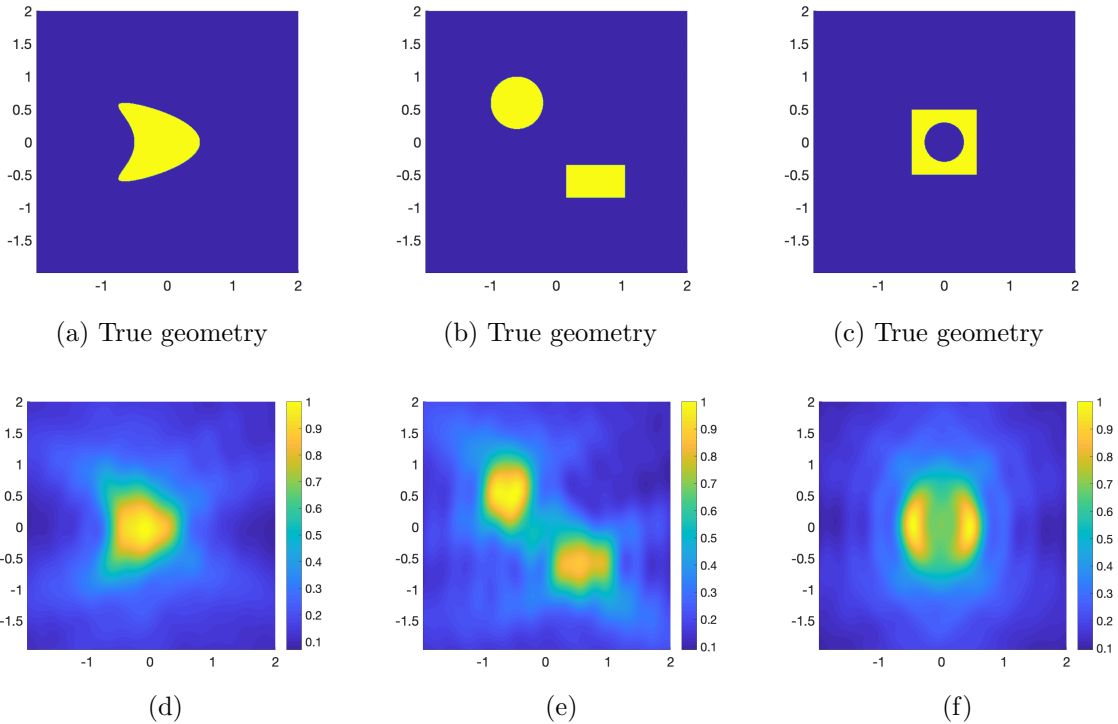


Figure 4: Reconstruction with partial limited aperture near-field data. There is 30% noise added to the data and $k = 8$.

Three data sets were investigated: the first one named *dielTM_dec4f.exp* is associated with a dielectric target that is a de-centered circular cross section of radius 15 mm, and the second one is *rectTM_cent.exp* concerning a centered rectangular cross section (dielectric material) of dimensions $25.4 \times 12.7 \text{ mm}^2$. The last one named *uTM_shaped.exp* is associated with a metallic U-shaped object of size $50 \times 80 \text{ mm}^2$. A detailed description of the experimental setup can be found in [3].

We rescaled 40 mm to be 1 unit of length in our MATLAB simulations. Measurement distance from the origin is about 0.76 m which is close to 19 in our simulation. The data are clearly measured in a far-field regime. The data matrix size is 72 (receivers) \times 36 (incident sources), where 72 receivers are distributed at the angular range from 60° to 300° in steps of 5° and the rotation of the target for the source is from 0° to 350° in steps of 10° . For the convenience of the readers we create the geometry of these targets in Figures 5(a, b, c) so that we can compare with the reconstruction results.

We consider the wave frequency 8 GHz for the data sets (wave number k is about 6.7 which means the wavelength is about 0.93). Since we only have the scattered wave data on a circle in a far field regime, we use $I_{\text{far}}(z)$ to reconstruct the targets. We compute $I_{\text{far}}(z)$ at 64×64 sampling points in the search domain $(-2.5, 2.5)^2$. There is no need for any regularization or any further processing for the experimental data. In Figures 5 we can see that the indicator function $I_{\text{far}}(z)$ is able to reconstruct the targets with reasonable

accuracy.

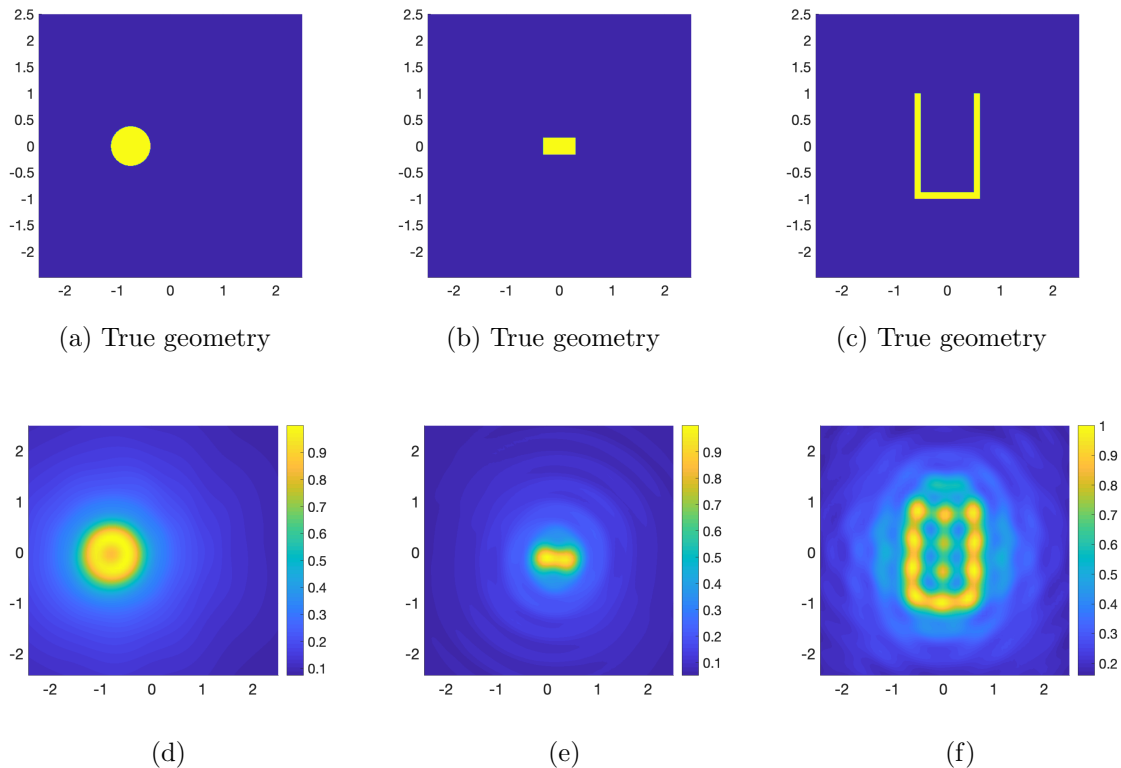


Figure 5: Reconstruction with experimental data from the Fresnel Institute using $I_{\text{far}}(z)$.

Acknowledgement. The work of the authors was partially supported by NSF grant DMS-2208293.

References

- [1] M. Akinici, M. Cayoren, and I. Akduman. Near-field orthogonality sampling method for microwave imaging: Theory and experimental verification. *IEEE Trans. Microw. Theory Tech.*, 64:2489, 2016.
- [2] L. Audibert and H. Haddar. A generalized formulation of the linear sampling method with exact characterization of targets in terms of farfield measurements. *Inverse Problems*, 30:035011, 2014.
- [3] Kamal Belkebir and Marc Saillard. Special section: Testing inversion algorithms against experimental data. *Inverse Problems*, 17(6):1565–1571, nov 2001.

- [4] F. Cakoni, D. Colton, and H. Haddar. *Inverse Scattering Theory and Transmission Eigenvalues*. SIAM, 2016.
- [5] F. Cakoni, D. Colton, and P. Monk. *The Linear Sampling Method in Inverse Electromagnetic Scattering*. SIAM, 2011.
- [6] D. Colton, J. Coyle, and P. Monk. Recent developments in inverse acoustic scattering theory. *SIAM Review*, 42:396–414, 2000.
- [7] D. Colton and A. Kirsch. A simple method for solving inverse scattering problems in the resonance region. *Inverse Problems*, 12:383–393, 1996.
- [8] D. Colton and R. Kress. *Inverse Acoustic and Electromagnetic Scattering Theory*. Springer, New York, 3rd edition, 2013.
- [9] R. Griesmaier. Multi-frequency orthogonality sampling for inverse obstacle scattering problems. *Inverse Problems*, 27:085005, 2011.
- [10] I. Harris and A. Kleefeld. Analysis of new direct sampling indicators for far-field measurements. *Inverse Problems*, 35:054002, 2019.
- [11] I. Harris and D.-L. Nguyen. Orthogonality sampling method for the electromagnetic inverse scattering problem. *SIAM J. Sci. Comput.*, 42:B72–B737, 2020.
- [12] I. Harris, D.-L. Nguyen, and T.-P. Nguyen. Direct sampling methods for isotropic and anisotropic scatterers with point source measurements. *Inverse Probl. Imaging*, 16(5):1137–1162, 2022.
- [13] M. Ikehata. Reconstruction of the shape of the inclusion by boundary measurements. *Commun. Part. Diff. Eq.*, 23:1459–1474, 1998.
- [14] K. Ito, B. Jin, and J. Zou. A direct sampling method to an inverse medium scattering problem. *Inverse Problems*, 28:025003, 2012.
- [15] K. Ito, B. Jin, and J. Zou. A direct sampling method for inverse electromagnetic medium scattering. *Inverse Problems*, 29:095018, 2013.
- [16] S. Kang and M. Lambert. Structure analysis of direct sampling method in 3D electromagnetic inverse problem: near- and far-field configuration. *Inverse Problems*, 37:075002, 2021.
- [17] S. Kang, M. Lambert, and W.-K. Park. Direct sampling method for imaging small dielectric inhomogeneities: analysis and improvement. *Inverse Problems*, 34:095005, 2018.
- [18] A. Kirsch. Characterization of the shape of a scattering obstacle using the spectral data of the far field operator. *Inverse Problems*, 14:1489–1512, 1998.

- [19] A. Kirsch and N.I. Grinberg. *The Factorization Method for Inverse Problems*. Oxford Lecture Series in Mathematics and its Applications 36. Oxford University Press, 2008.
- [20] T. Le, D.-L. Nguyen, H. Schmidt, and T. Truong. Imaging of 3D objects with experimental data using orthogonality sampling methods. *Inverse Problems*, 38:025007, 2022.
- [21] A. Lechleiter and D.-L. Nguyen. A trigonometric Galerkin method for volume integral equations arising in TM grating scattering. *Adv. Comput. Math.*, 40:1–25, 2014.
- [22] X. Liu. A novel sampling method for multiple multiscale targets from scattering amplitudes at a fixed frequency. *Inverse Problems*, 33:085011, 2017.
- [23] D.-L. Nguyen. Direct and inverse electromagnetic scattering problems for bi-anisotropic media. *Inverse Problems*, 35:124001, 2019.
- [24] W.-K. Park. Direct sampling method for retrieving small perfectly conducting cracks. *J. Comput. Phys.*, 373:648–661, 2018.
- [25] R. Potthast. A fast new method to solve inverse scattering problems. *Inverse Problems*, 12:731–742, 1996.
- [26] R. Potthast. A survey on sampling and probe methods for inverse problems. *Inverse Problems*, 22:R1–R47, 2006.
- [27] R. Potthast. A study on orthogonality sampling. *Inverse Problems*, 26:074015, 2010.
- [28] S. Vanska. Stationary waves method for inverse scattering problems. *Inverse Probl. Imaging*, 2:577–586, 2008.